Chapter 3

Dumbbell defect containing Chromium-rich Lithium-vacant Layered $Li_yCr_{1-x}Fe_xO_2$ ($y \leq 1$, $0 \leq x \leq 0.2$): An Unexplored and Highly Efficient Electrocatalyst for Oxygen Evolution Reaction

Chapter 3

Dumbbell defect containing Chromium-rich Lithium-vacant Layered $Li_yCr_{1-x}Fe_xO_2$ ($y \leq 1$, $0 \leq x \leq 0.2$): An Unexplored and Highly Efficient Electrocatalyst for Oxygen Evolution Reaction

3.1 Introduction

Oxygen electrochemistry plays a critical role in the energy storage and conversion technologies, particularly in the field of metal-air batteries, fuel cells, and water electrolyzers. The efficiency of these energy technologies is strongly limited for oxygen evolution reaction (OER) due to a high overpotential associated with its sluggish kinetics [1, 2]. The naturally occurring $CaMn_4O_x$ clusters (PS II water-oxidizing complex) are capable to perform water oxidation at very low overpotentials with significant turnover frequency [3-5]. However, these naturally occurring enzymes are hardly used in commercial electrochemical devices due to their instability under operating conditions [6]. Up to now, the noble-metal-based oxides (such as IrO_2 and RuO_2) are employed as the best OER catalysts, reported with very low overpotentials, but their high cost, low abundance, and poor stability in alkaline electrolytes restrict their practical application [7]. Therefore, it is imperative to design and develop alternative OER electrocatalysts based on low-cost and earth-abundant elements, significantly with low overpotentials. In the past few years, a variety of OER catalysts based on 3*d* transition metal (Ni, Co, Fe, Mn) oxides, hydroxides, and oxyhydroxides have been widely investigated in alkaline electrolytes [8-12]. The highly oxidized redox couples in transition metal oxides such as $Co^{3+/4+}$, $Ni^{3+/4+}$, $Mn^{3+/4+,}$ and $Fe^{3+/4+}$ are recognized as active centers for OER. Several spinel oxides (e.g., Co_3O_4 and $NiCo_2O_4$) [13] and perovskites (e.g., $Ba_{0.5}Sr_{0.5}Co_{0.8}Fe_{0.2}O_{3-\delta}$) [14] have proven to be promising OER catalysts. Moreover, it is noted that various layered and lithiated spinel type $LiMO_2$ (M = Ni, Co, Fe, Mn) oxides that are widely applied as cathode

materials in Li-ion batteries, have recently been investigated as active OER candidates in alkaline electrolytes. One of the interesting and technically relevant features of these materials is to tune the oxidation state of transition metal ions by varying the lithium content [15-18]. For example, the low-temperature phase of $LiCoO_2$ (LT-$LiCoO_2$), and its chemically de-lithiated analogue (LT-$Li_{0.5}CoO_2$ by NO_2BF_4) have been stated to be good catalysts for the OER and ORR than its high-temperature phase (HT-$LiCoO_2$) [17]. A similar result has also been reported by Lu et al. with the electrochemical de-lithiation process, where the HT-$LiCoO_2$ was charged to 4.3 V (vs. Li/Li^+) which would significantly improve its catalytic activity by tuning the oxidation state of $Co^{3+/4+}$ [18]. In recent years, the systematic Ni-rich layered $LiNi_{1-x}M_xO_2$ (M = Mn, Fe, Co) oxides have revealed that the catalytic activity can be tuned by varying the Ni content, nature of the transition-metal dopant, lithium content, and degree of cation ordering between Li and Ni/M [19]. Furthermore, the doping of Al [20] and Fe [21] in $LiNiO_2$ can significantly improve the OER activity by tuning the valence state of Ni from Ni^{2+} to Ni^{3+}. However, to the best of our knowledge, Cr has rarely been explored as an OER electrocatalyst [22, 23]. Despite exploration of layered $LiMO_2$ (M = Mn, Fe, Co, and Ni) phases, no studies are made yet on layered $LiCrO_2$; an inactive cathode in Li-ion batteries resulting in the formation of the stable dumbbell defect structure due to Cr^{6+} ion at interstitial sites during charging that block Li^+-ion conduction pathways. In layered $LiMO_2$ materials, transition metals (M_{oct}) migrate into the Li layer through intermediate tetrahedral sites creating dumbbell defects; in this migration process, each $M_{oct} \rightarrow M_{tet}$ defect is stabilized by one $Li_{oct} \rightarrow Li_{tet}$ defect immediately below the vacated transition metal site. This defect configuration, consisting of $M_{tet}–M_{vac}–Li_{tet}$, is called a dumbbell defect [24]. Just recently, an amorphous γ-CrOOH was developed as a bifunctional electrocatalyst for overall water splitting for the first time [25(a)]. Gao et al. have recently verified that the in-situ synthesized Fe-doped CrOOH nanosheets as

highly efficient OER electrocatalysts [25(b)]. However, the pure Cr-based electrocatalysts for water oxidation are still a research blank.

We believed that the dumbbell defect containing layered $LiCrO_2$ can show superior and stable OER activity due to the presence of Cr^{6+} ion at interstitial sites that facilitates -Cr-O-OH formation, important for oxygen evolution in basic media and higher stability of the catalyst can be the result of thermodynamically stable dumbbell defect containing layered structure formation. We have successfully synthesized a series of dumbbell defects containing layered $Li_yCr_{1-x}Fe_xO_2$ ($y \leq 1$, $0 \leq x \leq 0.2$) with different Fe doping amounts to investigate their electrocatalytic performance towards the OER in alkaline solution for the first time. Combined with X-ray diffraction (XRD) and XPS data, it was found that the better cation mixing due to O3-type layered rhombohedral structure formation and formation of Cr^{6+} ion interstitials in the Li layer increase that varies with the Fe doping in $Li_yCr_{1-x}Fe_xO_2$ ($y \leq 1$, $0 \leq x \leq 0.2$), and the best OER activity is achieved on $Li_{0.6}Cr_{0.9}Fe_{0.1}O_2$ (LCFO-10) with a Tafel slope of 50 mV dec^{-1} and an overpotential of 311 mV at a current density of 10 mA cm^{-2}, better than that of commercial RuO_2 (benchmark catalyst), measured under similar experimental conditions. Furthermore, the leaching experiment of LCFO-10 in KOH and HCl solution has also been conducted to see their effect on its electrocatalytic OER performance and stability of the catalyst.

3.2 Experimental section

3.2.1 Material synthesis

A solid-state ceramic synthesis route was adopted to synthesize crystalline $LiCr_{1-x}Fe_xO_2$ ($0 \leq x \leq 0.2$) powder. A stoichiometric amount of precursor compounds such as Li_2CO_3 (Sigma Aldrich, ≥ 99 %), Cr_2O_3 (Sigma Aldrich, ≥ 98 %), and Fe_2O_3 (Sigma Aldrich, ≥ 99.99 %) were taken in an agate mortar-pestle and ground for half an hour to form a homogeneous mixture.

The sample mixture was first heated at 550 ℃ for 6 h and then calcined at 800 ℃ for 30 h in an oxygen environment with intermediate grinding to get single-phase material. The oxygen environment was specially created to obtain the dumbbell defects containing structure by facilitating the oxidation of Cr^{3+} ions into Cr^{6+}. The samples were further denoted as LCFO-0, LCFO-5, LCFO-10, LCFO-15, and LCFO-20 for 0, 5, 10, 15, and 20% Fe-doped $LiCrO_2$, respectively, in the thesis. The electrochemical activity of the synthesized catalyst was compared with commercial RuO_2 (Sigma Aldrich, 99%, a well know benchmark catalyst for Oxygen evolution reaction) in the same condition of the experiment.

3.3 Results and discussion

3.3.1 XRD studies and Rietveld refinement

Figure 3.1 shows the XRD patterns of the $Li_yCr_{1-x}Fe_xO_2$ ($y \leq 1$, $0 \leq x \leq 0.2$) samples recorded in the 2θ range of 10−80º. The sharp and well-separated diffraction peaks in the XRD pattern indicate the crystalline nature of the material and are indexed with the standard rhombohedral phase (Space Group: R-3m) of $LiCrO_2$ (JCPDS No. 00-024-0600). No impurity peaks were detected up to 10 % iron doping in the $LiCrO_2$ structure. However, a small impurity peak of iron oxide starts appearing when the dopant concentration is further increased that suggests only 10% Fe can replace the Cr atom in the $LiCrO_2$. It has been reported earlier that the intensity ratio of (003) to (104) peak serves as an indicator of the degree of cation intermixing in layered $LiCrO_2$; a lower value of I_{003}/I_{104} corresponds to a higher degree of cation intermixing [26]. The intensity ratio of (003)/(104) peak for all synthesized LCFOs was found to be in order: LCFO-10 (1.02) < LCFO-5 (1.15) < LCFO-15 (1.18) < LCFO-20 (1.21) < LCFO-0 (1.29) that indicates a high degree of cation intermixing for LCFO-10.

Further, Rietveld refinement of LCFO-0, LCFO-10 and LCFO-20 was performed by taking Pseudo-Voigt as peak pofile function and R-3m space group, shown in **Figure 3.2**. The

refinement results along with their reliability factors (R_{bragg}, R_f, and χ^2) were listed in **Table 3.1**. From the refinement, it has been emphasized that the amount of Cr that can intermix in the Li layer is highest in the case of LCFO-10. These results coincide with our XRD results obtained from the intensity ratio of the (003)/(104) peak. **Figure 3.3(a-c)** represents the crystal structure of $Li_yCr_{1-x}Fe_xO_2$ which shows a layered rhombohedral structure containing dumbbell defects (interstitial site occupied by Cr^{6+} ions) in the HCP lattice. In the layered $Li_yCr_{1-x}Fe_xO_2$, doping of Fe significantly increases the cation-mixing and partial Li-vacancy in the structure. The doping of Fe substantially causes the partial oxidation of Cr^{3+} to Cr^{6+}, and the generated Cr^{6+} is further migrated to the tetrahedral/interstitial site of the Li-layer (cation-mixing), creating dumbbell defects in the layered $Li_yCr_{1-x}Fe_xO_2$, as shown in **Figure 3.3(a-c)**.

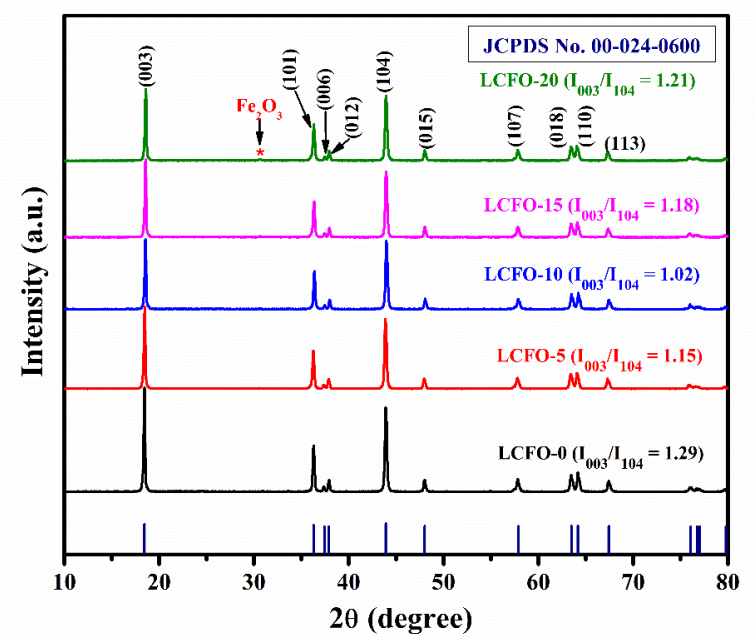

Figure 3.1 XRD pattern of different synthesized LCFO samples.

Table 3.1 Structural parameters of LCFO-0, LCFO-10, and LCFO-20 based on Rietveld refinement.

Catalysts	a = b (Å)	c (Å)	χ^2	R_f	R_{bragg}	I_{003}/I_{104}	Cr in Li layer (%)
LCFO-0	2.9005	14.4308	2.03	4.66	5.59	1.29	2
LCFO-10	2.9006	14.4283	2.17	7.89	8.91	1.02	14
LCFO-20	2.9154	14.4681	2.39	8.3	9.28	1.21	5

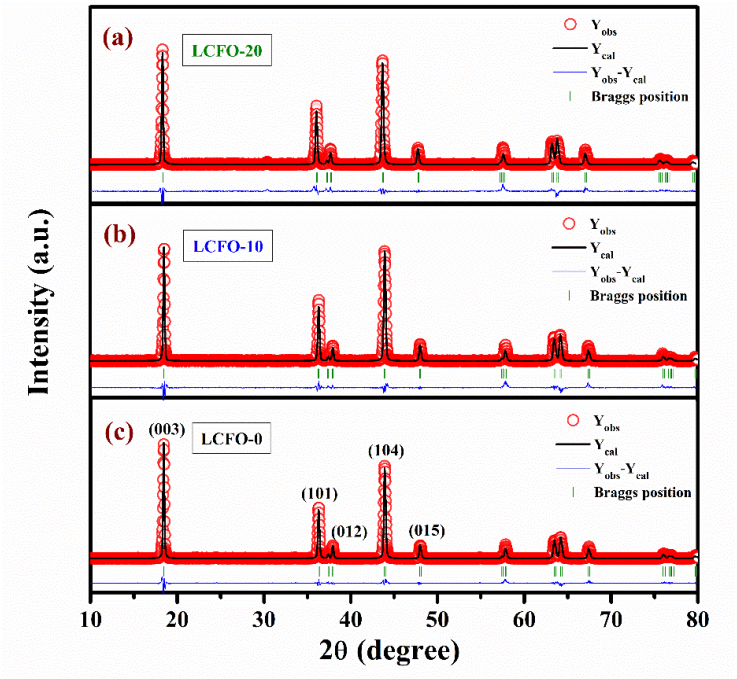

Figure 3.2 Rietveld refined powder XRD patterns of **(a)** LCFO-0, **(b)** LCFO-10 and **(c)** LCFO-20.

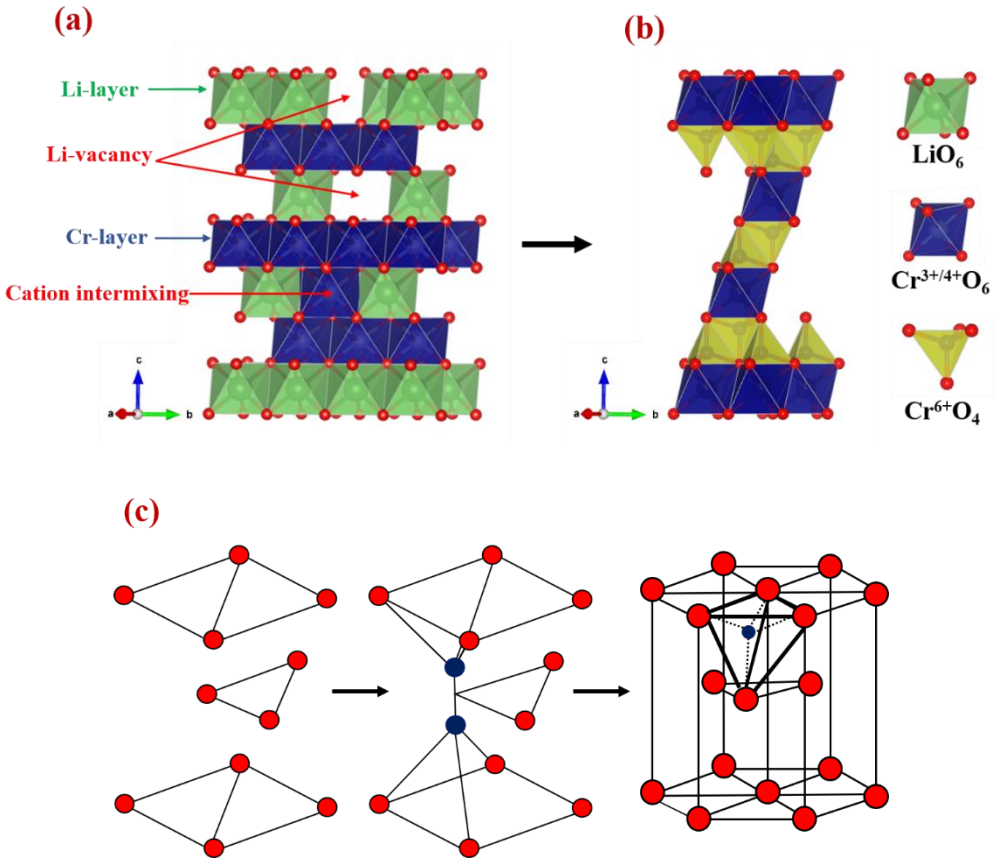

Figure 3.3 Crystal structure of Fe doped $LiCrO_2$: **(a)** layered structure having space group R-3m, **(b)** interstitial Cr^{6+} ions occupied dumbbell defect containing structure and **(c)** lattice space for dumbbell defects in HCP lattice.

3.3.2 XPS and ICP analysis

The X-ray photoelectron spectroscopy (XPS) measurements were performed to analyze the electronic structure of the materials and study the oxidation state of the elements (Cr, Fe, Li, and O) present in electrocatalysts. **Figure 3.4(a, b)** represents the Cr(2*p*) core level spectra of LCFO-0 and LCFO-10 that consist of Cr doublet corresponding to the binding energies of Cr($2p_{3/2}$) and Cr($2p_{1/2}$). Further, these two peaks (Cr $2p_{3/2}$ and Cr $2p_{1/2}$) were de-convoluted to get the reference peak positions of Cr(2*p*). The binding energies at ~575.9 ($2p_{3/2}$) and ~585.8 eV ($2p_{1/2}$) were assigned to Cr^{3+} whereas the binding energies at ~577.8 ($2p_{3/2}$) and ~587.6 eV ($2p_{1/2}$) were assigned to Cr^{6+} [27]. After de-convolution, the observed ratio between the fractional composition of Cr^{3+} to Cr^{6+} in LCFO-0 is 0.89: 0.11, and in LCFO-10 is 0.85: 0.15. This result confirms that doping of Fe is more prone to keep Cr in its higher oxidation state. **Figure 3.4c** represents the Fe(2*p*) core level spectra of LCFO-10, consisting of two peaks centered at ~711.26 eV (with a satellite at 718.7 eV) and at ~724.72 eV (with a satellite at 732.81 eV) corresponding to Fe($2p_{3/2}$) and Fe($2p_{1/2}$), which confirms that Fe is present only in +3 oxidation state. The Li(1*s*) and O(1*s*) spectra of LCFO-0 and LCFO-10 are also given in **Figure 3.4(d, e)** and **Figure 3.4(f, g)**, respectively. The binding energy values of Li(1*s*) at ~54.5 and ~55.9 eV confirms the presence of lattice lithium in two different cation environments (octahedral Cr^{3+} polyhedra and interstitial Cr^{6+} tetrahedra, respectively). The deconvoluted O(1*s*) spectra consist of two peaks centered at ~529.46 and ~531.27 eV confirming the presence of lattice oxygen (O^{2-}) and "non-stoichiometric" surface oxygen or hydroxide (OH^-), respectively [28]. The presence of Li, Cr, Fe, and O in the XPS spectrum indicates the successful formation of dumbbell defects containing layered Fe-doped $LiCrO_2$ compound. Relative surface concentrations of Li: Cr and Li: Cr: Fe in $LiCrO_2$ and $LiCr_{0.9}Fe_{0.1}O_2$ was made using the intensities of Cr(2*p*), Fe(2*p*), and Li(1*s*) peaks. The relative surface concentration is calculated from the formula [29].

$$Relative\ concentration, C_M = \frac{I_M/\lambda_M\sigma_M D_M}{\sum(I_M/\lambda_M\sigma_M D_M)} \quad (3.1)$$

where I_M is the integrated intensity of the core levels (M = Cr ($2p$), Fe($2p$), and Li($1s$), λ_M is the mean escape depths of the respective photoelectrons, σ_M is the photoionization cross-section, and D_M is the geometric factor. The photoionization cross-section values were taken from Scofield's data [30] and the mean escape depths were taken from Penn's data [31]. The geometric factor was taken as 1 because the maximum intensity in this spectrometer is obtained at 90º. The surface concentrations of Li, Cr, and Fe were found in the ratio of 0.6: 0.89: 0.11 in $Li_yCr_{0.9}Fe_{0.1}O_2$, and the Li: Cr ratio was found to be 0.67: 1 in Li_yCrO_2.

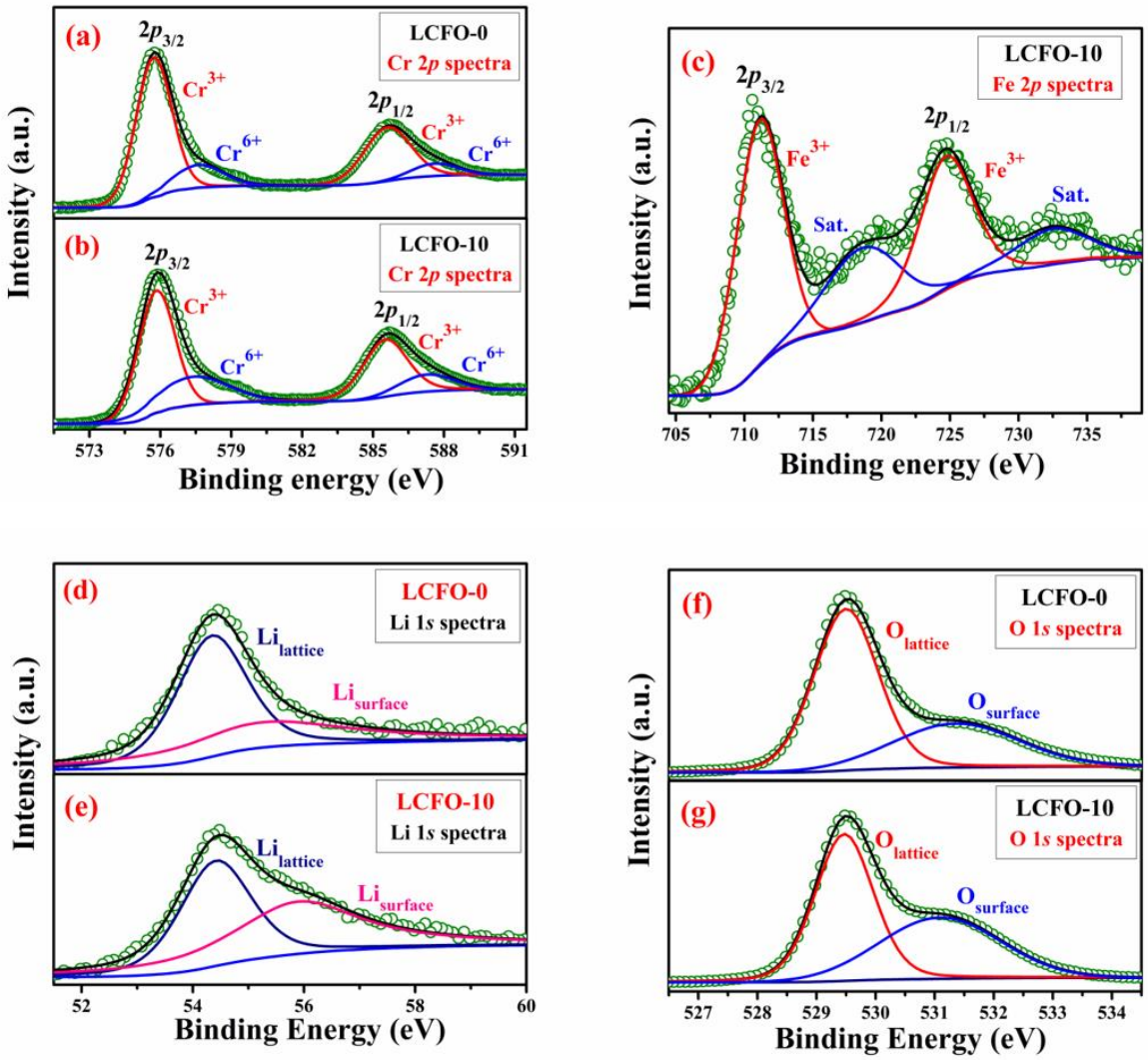

Figure 3.4 XPS spectra of **(a, b)** Cr(2p), **(c)** Fe(2p), **(d, e)** Li(1s) and **(f, g)** O(1s).

Further, the relative concentration of Cr, Fe, and Li in the samples was also confirmed by the ICP-MS study using Inductively Coupled Plasma Mass Spectrometry (ICP-MS), (make: Agilent 7800 ICP-MS mainframe). The nominal (desired) and actual composition (obtained from the ICP-MS analysis) of all synthesized $Li_yCr_{1-x}Fe_xO_2$ ($y \leq 1$, $0 \leq x \leq 0.2$) catalysts are listed in **Table 3.2**. The observed value from the XPS study matches very well with the elemental ratios obtained from the ICP-MS study. Thus, the formula of the compound along with the electronic structure of the electrocatalysts can be represented as $Li_{0.67}Cr^{3+}_{0.89}Cr^{6+}_{0.11}O_2$ and $Li_{0.6}(Cr^{3+}_{0.85}Cr^{6+}_{0.15})_{0.9}Fe_{0.1}O_2$ or $Li_{0.6}Cr^{3+}_{0.76}Cr^{6+}_{0.14}Fe^{3+}_{0.1}O_2$. Thus combined XRD and XPS study confirms the formation of lithium vacant chromium-rich dumbbell defect containing layered structure $Li_yCr_{1-x}Fe_xO_2$ ($y \leq 1$, $0 \leq x \leq 0.2$) due to occupancy of Cr^{6+} ions at interstitial tetrahedral sites present in hexagonal closed pack rhombohedral lattice. The presence of the chromate (CrO_4^{2-}) ion confirming the existence of Cr^{6+} ion in LCFO-10 lattice was examined through the FT-IR analysis of the samples presented in later studies.

Table 3.2. Molar ratios of Li, Cr, Fe in $Li_yCr_{1-x}Fe_xO_2$ ($y \leq 1$, $0 \leq x \leq 0.2$) from ICP analysis.

Nominal Composition	**ICP composition of $Li_yCr_{1-x}Fe_xO_2$ ($y \leq 1$, $0 \leq x \leq 0.2$)**		
	Li	**Cr**	**Fe**
$LiCrO_2$	0.67	1.00	0.00
$LiCr_{0.95}Fe_{0.05}O_2$	0.65	0.95	0.05
$LiCr_{0.9}Fe_{0.1}O_2$	0.60	0.90	0.10
$LiCr_{0.85}Fe_{0.15}O_2$	0.63	0.85	0.15
$LiCr_{0.8}Fe_{0.2}O_2$	0.65	0.80	0.20

3.3.3 Microstructural analysis

The morphology and particle size distribution of LCFO-10 is determined from scanning electron micrographs. The SEM image of LCFO-10, shown in **Figure 3.5(a, b)** indicates that the particles are uniformly distributed in the entire region of the micrograph.

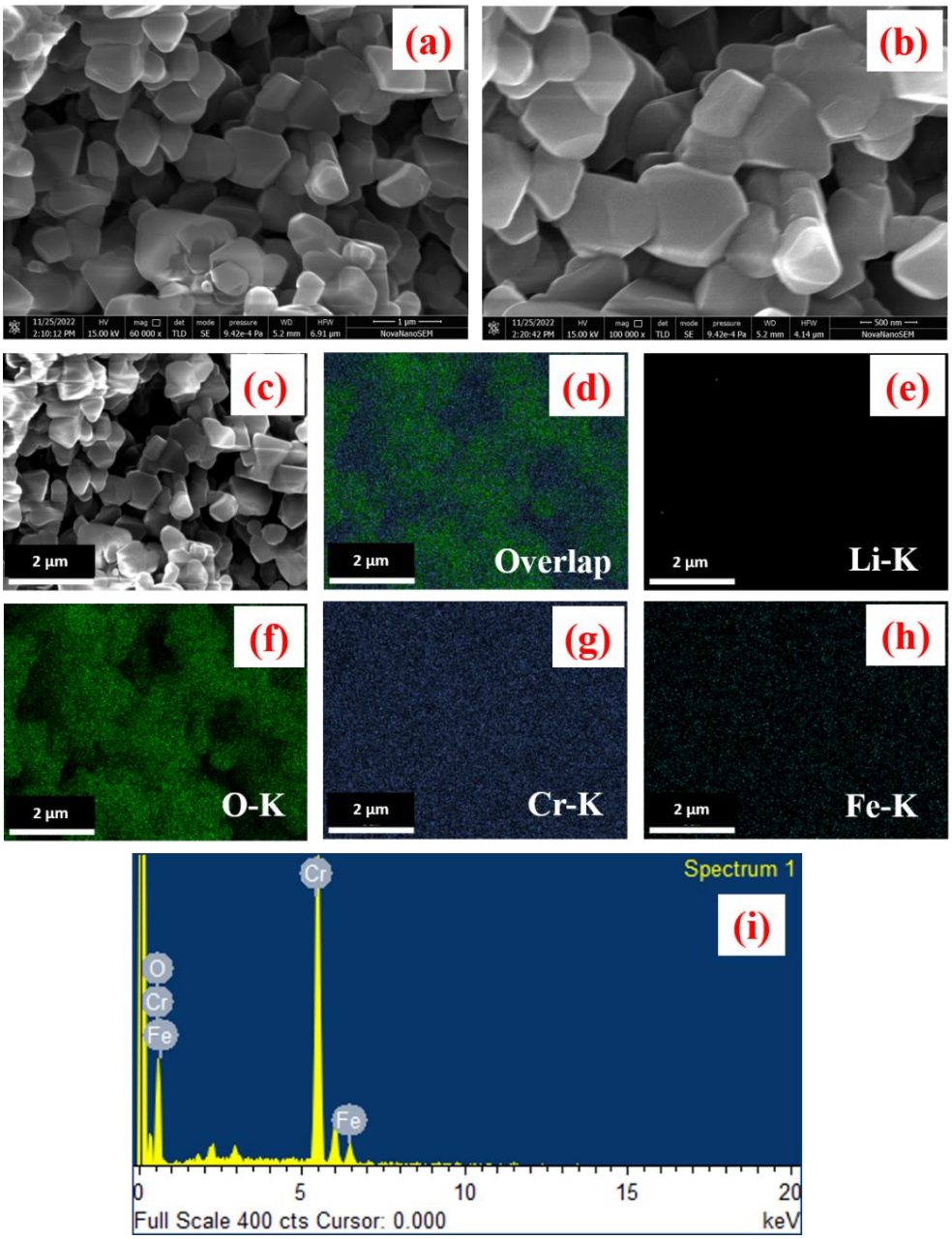

Figure 3.5 (a, b) SEM micrograph of LCFO-10 (scale bar: **(a)** 1 µm with 60,000x magnification and **(b)** 500 nm with 1,20,000x magnification), **(c)** area used for EDX mapping, **(d-h)** EDX mapping of overall and individual elements (Li, O, Cr, and Fe, respectively) and **(i)** EDX spectrum of LCFO-10. Note: Li signals are absent in EDX mapping as EDX techniques are not capable of recording signals for the Li core level.

Figure 3.5c shows the area of the sample on which EDX mapping was carried out to get the elemental uniformity and composition of the material. **Figure 3.5(d-h)** shows the different color elemental mapping of Li, Cr, Fe, and O atoms. Since the excitation energy of the Li

element is low, therefore, it is not possible to detect the Li in the sample by SEM-EDX. The energy dispersive spectra (shown in **Figure 3.5i)** confirm only the presence of Cr, Fe, and O atoms and the data confirms that the obtained elemental composition (Cr: Fe = 0.89: 0.11) in LCFO-10 is almost the same as the nominal composition taken for the synthesis.

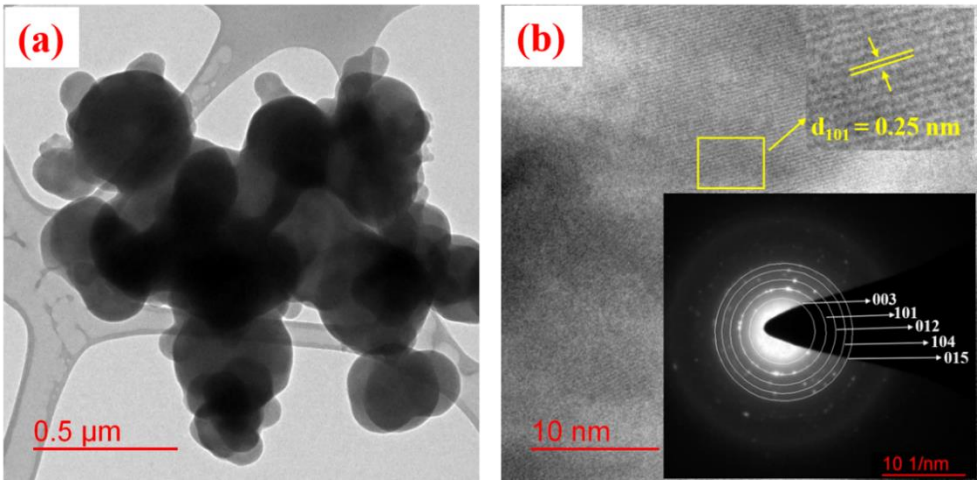

Figure 3.6 (a) Bright field TEM image and **(b)** HR-TEM with interplanar d-spacing of (101) plane, (inset: the SAED pattern) of LCFO-10.

Further, the bright-field TEM image of LCFO-10 (shown in **Figure 3.6a)** indicates inhomogeneous agglomerated particles, whose size ranges from 100 to 250 nm. The high resolution-TEM image, **Figure 3.6b**, displays lattice fringes with inter-planar d-spacing of 0.25 nm corresponding to the (101) plane. The presence of distinct rings in the selected area electron diffraction (SAED) pattern, as shown in the inset of **Figure 3.6b**, indicates that the synthesized LCFO-10 is polycrystalline and the diffraction rings from inside to outside represent the (003), (101), (012), (104) and (015) plane of rhombohedral $LiCrO_2$, which are in close agreement with the XRD results.

3.3.4 Electrochemical studies

3.3.4.1 OER performances of synthesized catalysts

The electrochemical performance of $Li_yCr_{1-x}Fe_xO_2$ ($y \leq 1$, $0 \leq x \leq 0.2$) catalysts towards the OER were investigated in O_2-saturated 1 M KOH at a scan rate of 5 mV s^{-1} in a three-electrode

setup. Before collecting the data, the working electrode was first scanned for several cycles at a scan rate of 100 mV s^{-1} in the range of 1.0 – 1.8 V vs. RHE to obtain a stable current. The LSV curves, shown in **Figure 3.7a,** represent the OER performance of all the synthesized LCFO catalysts, which follow the order: LCFO-20 < LCFO-0 < LCFO-15 < LCFO-5 < LCFO-10. From **Figure 3.7a**, it has been observed that the catalytic activity of LCFO increases with increasing the Fe concentration up to 10 %, after that the OER activity starts decreasing. The required overpotential to achieve a current density of 10 mA cm^{-2} (on a basis of 10% solar-to-fuel conversion efficiency) for LCFO-0, LCFO-5, LCFO-10, LCFO-15, and LCFO-20 was found to be 374, 347, 311, 364 and 383 mV, respectively, shown in **Figure 3.7b**. The Tafel slope, which describes the influence of potential by current density, is an important factor to evaluate the reaction kinetics. **Figure 3.7c** shows the Tafel plot of various LCFOs and the slope values obtained for LCFO-0, LCFO-5, LCFO-10, LCFO-15, and LCFO-20 are approximately 74, 57, 50, 70, and 65 mV dec^{-1}, respectively. The lowest Tafel slope of LCFO-10 (50 mV dec^{-1}) indicates its much faster reaction kinetics among all the LCFOs. Further, the impedance studies were conducted in a frequency range of 0.1 Hz –100 kHz at a potential of 1.5 V vs. RHE with an AC amplitude of 10 mV to measure the charge transfer resistance of our synthesized catalysts, as shown in **Figure 3.7d**. An equivalent circuit fit of the EIS data is also given in the inset of **Figure 3.7d**, that contains a solution resistance (R_s), a charge-transfer resistance (R_{ct}), and a constant-phase element (CPE). The Nyquist semicircle loop diameter at the high-frequency region represents the charge-transfer resistance (R_{ct}), an important parameter that decides the superiority of a catalyst for the OER process. The optimum concentration of Fe (10 %) in $LiCrO_2$ catalyst can significantly reduce the R_{ct} value that follows the order: LCFO-10 (11.27 Ω) < LCFO-5 (21.55 Ω) < LCFO-15 (31.11 Ω) < LCFO-0 (37.03 Ω) < LCFO-20 (47.26 Ω). The lowest R_{ct} value of LCFO-10 (11.27 Ω) indicates that it has much faster charge transfer kinetics during the catalytic process among all LCFOs.

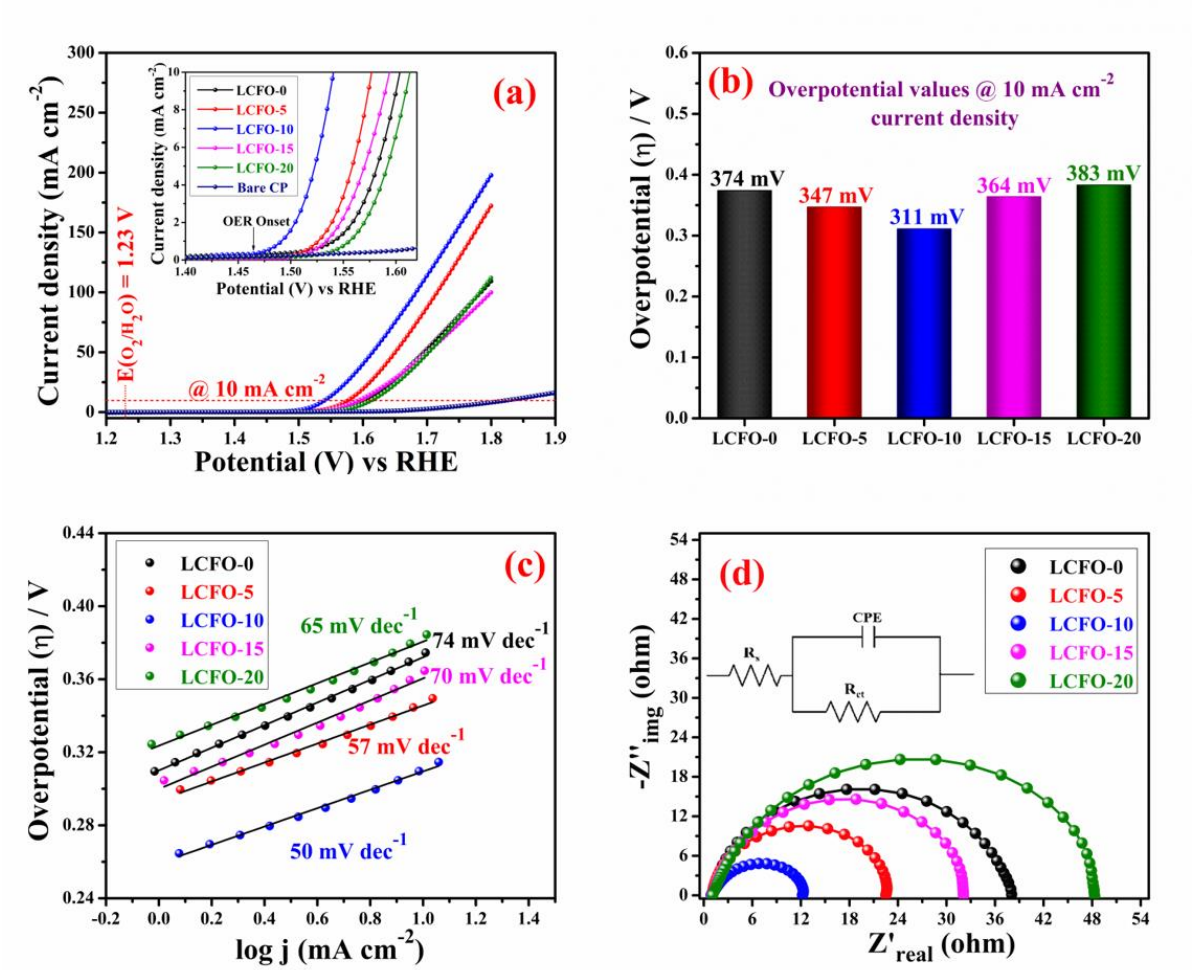

Figure 3.7 OER performance of $Li_yCr_{1-x}Fe_xO_2$ catalysts with various Fe contents ($y \leq 1$; $0 \leq x \leq 0.2$). **(a)** Linear sweep voltammograms taken at a scan rate of 5 mV s^{-1} in 1 M KOH, **(b)** Overpotentials at a current density of 10 mA cm^{-2}, **(c)** Tafel plots and **(d)** EIS recorded at 1.54 V vs. RHE.

3.3.4.2 Comparative OER study

In the present study, commercial RuO_2 (Sigma-Aldrich) was tested as a reference electrocatalyst under the same experimental conditions. **Figure 3.8a** represents the LSV curves of RuO_2 along with LCFO-10 to compare their OER performance in 1 M KOH. From **Figure 3.8a**, it was observed that RuO_2 requires 336 mV overpotential to reach a current density of 10 mA cm^{-2} (similar to Ananthraj's report) [32], whereas to achieve the same current density, LCFO-10 takes only 311 mV overpotential. Moreover, under an overpotential of 350 mV, the OER current density of LCFO-10 is 28.07 mA cm^{-2}, which is ~2 times higher than OER current

density observed with commercial RuO_2 (13.22 mA cm^{-2}), indicating its superior electrocatalytic activity.

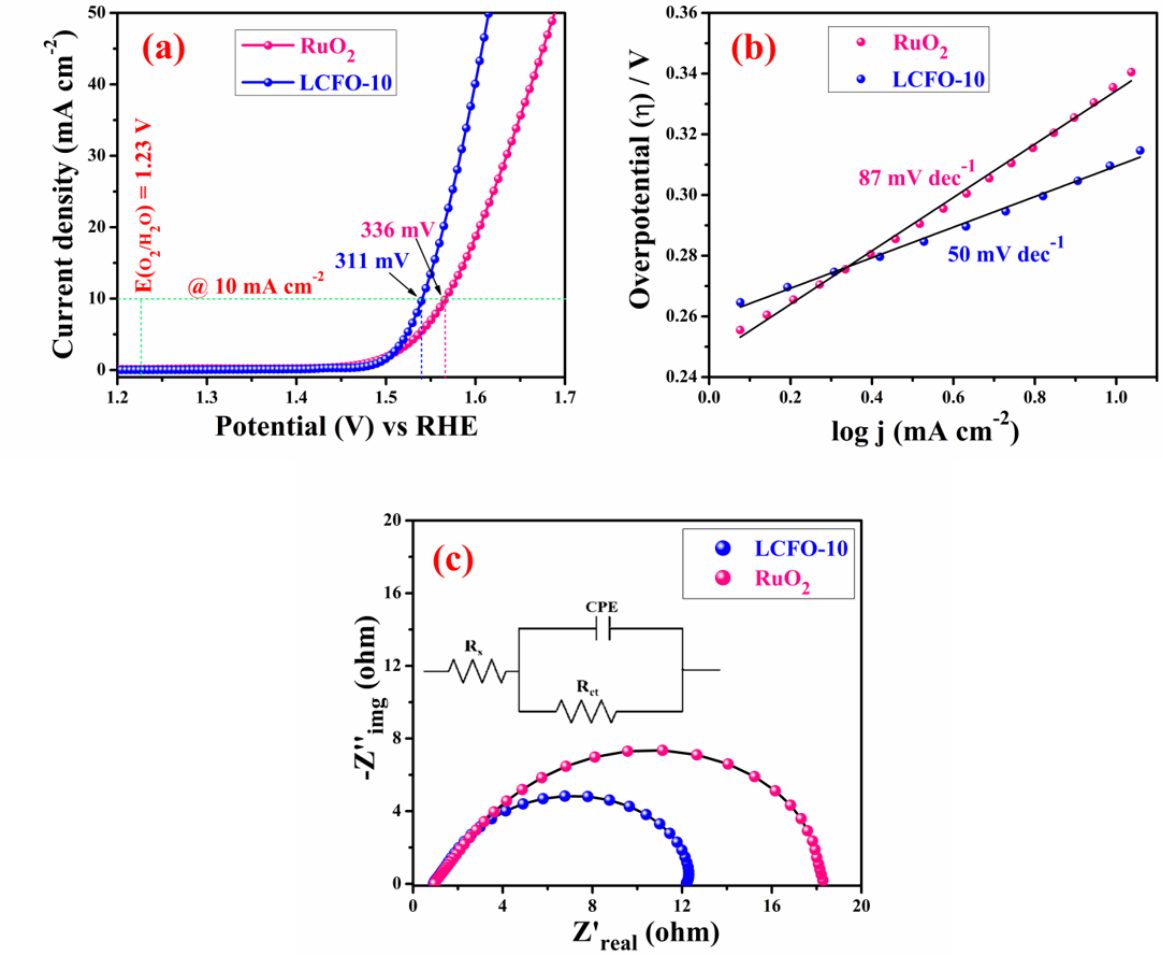

Figure 3.8 Comparison of OER performance of LCFO-10 with commercial RuO_2 as reference catalyst. **(a)** Linear sweep voltammograms recorded at 5 mV s^{-1} in 1 M KOH, **(b)** Tafel plots and **(c)** EIS measurement at an applied potential of 1.54 V vs. RHE.

Figure 3.8b represents the Tafel slope value of LCFO-10 (50 mV dec^{-1}) and RuO_2 (87 mV dec^{-1}) which is in accordance with their OER performances because a lower Tafel slope represents a faster OER kinetic rate. The activity of commercial RuO_2 provided in the present study is in close agreement with their earlier reports. The impedance spectra of LCFO-10 and commercial RuO_2 were also measured at a potential of 1.5 V vs RHE, shown in **Figure 3.8c**. A smaller semicircle loop represents the lower charge transfer resistance during the OER

process. The R_{ct} value of LCFO-10 is found to be 11.27 Ω, which is quite lower than RuO_2 (17.32 Ω), indicating its faster OER kinetic rate than the RuO_2 reference catalyst.

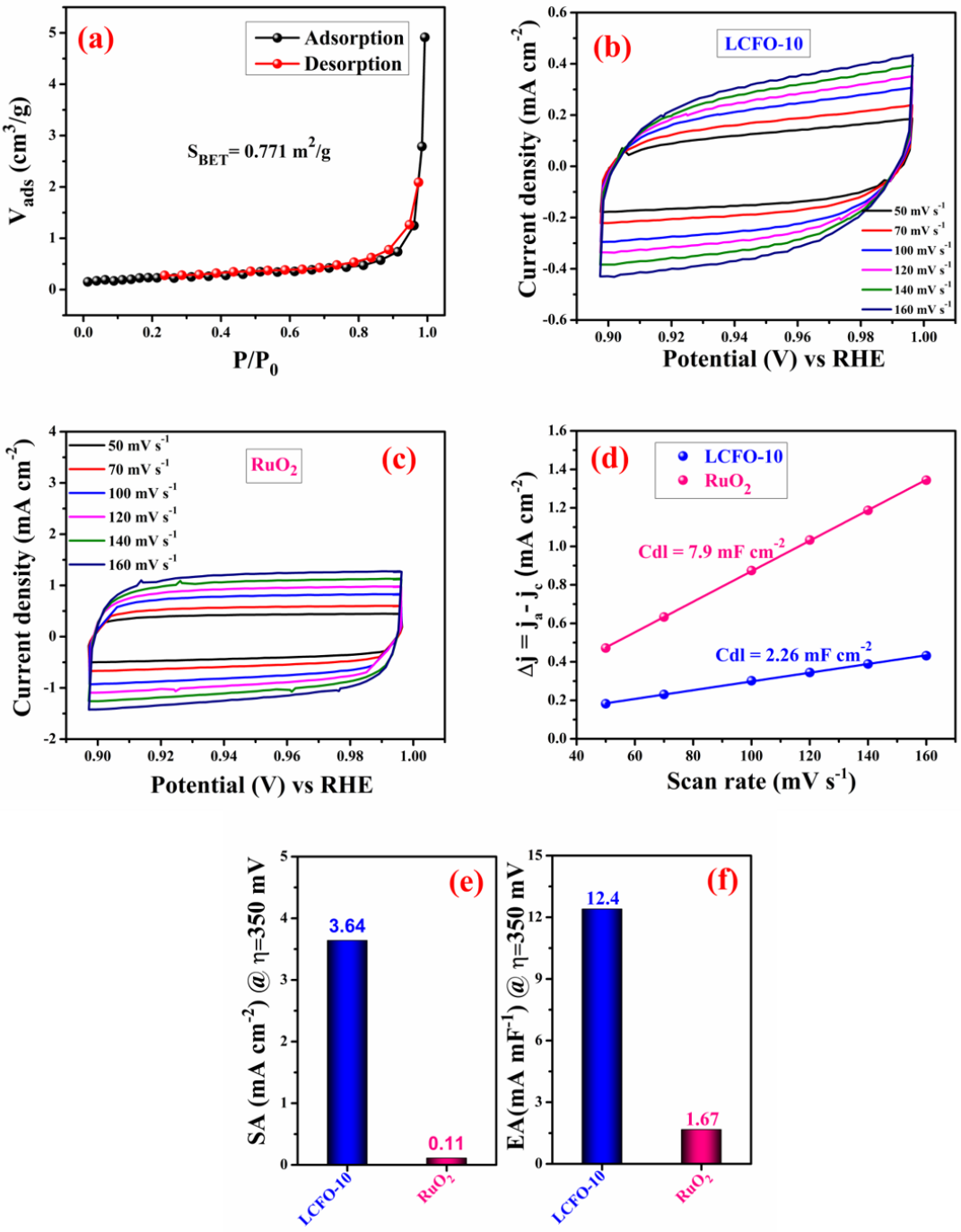

Figure 3.9 (a) N_2 adsorption/desorption isotherm curve of LCFO-10, **(b, c)** CV measurements in a non-faradic current region (0.9-1.0 V vs. RHE) at scan rates of 50, 100, 120, 140 and 160 mV s^{-1} of LCFO-10, and RuO_2, respectively, in 1 M KOH, **(d)** Plots of capacitive current density differences Δj vs. the scan rate for LCFO-10 and RuO_2 and **(e, f)** OER current density normalized by BET surface area (SA) and electric double-layer capacitance (EA) of LCFO-10 and RuO_2, respectively, at an overpotential of 350 mV.

Figure 3.9a represents the Brunauer-Emmett-Teller (BET) surface area measurement (N_2 adsorption/desorption isotherms) of LCFO-10 and from the isotherm, the specific surface area of LCFO-10 is found to be 0.771 m^2/g, while it is 11.38 m^2/g for commercial RuO_2 [33]. Further, the electrochemical active surface area (EA) of LCFO-10 and RuO_2 was estimated by measuring the electric double-layer capacitance in the non-faradaic region at various scan rates through cyclic voltammetry, as shown in **Figure 3.9(b, c).** The double layer capacitance (C_{dl}) of RuO_2 was measured to be 7.9 mF cm^{-2}, while that of LCFO-10, was only 2.26 mF cm^{-2}, (shown in **Figure 3.9d)**. The current density normalized by BET surface area (SA) of the LCFO-10 and the benchmark RuO_2 catalyst were also measured under an overpotential of 350 mV; the SA of LCFO-10 is 3.64 mA cm^{-2}, which is ~33 times higher than RuO_2 (0.11 mA cm^{-2}), as shown in **Figure 3.9e**. The current density normalized by electrochemical active surface area for LCFO-10 is 12.4 mA mF^{-1}, about 7.5 times that of RuO_2 (1.67 mA mF^{-1}), shown in **Figure 3.9f**. All the results confirm the superior OER activity of LCFO-10 compared to commercial RuO_2.

3.3.4.3 Mott-Schottky and flat-band potential

The excellent activity of LCFO-10 was further verified through the Mott−Schottky plot which provides basic information about the electrochemical interface potential between the electrode and electrolyte [34]. **Figure 3.10** shows the Mott−Schottky plot of LCFO-10 measured at 100 Hz in the range between 1.0 to 1.8 V vs. RHE; the negative slope of the plot indicates that LCFO-10 is a *p*-type (hole) semiconductor. Further, the flat band potential (E_{fb})of LCFO-10 can be estimated from the plot between $1/C^2$ vs. potential and the intercept made on the *x*-axis gives the value of E_{fb}. For a *p*-type semiconductor, if the onset potential E_{onset} is greater than E_{fb}, a high hole concentration at the electrode region has been generated, which favors the OER process. From **Figure 3.10**, the E_{fb} of LCFO-10 was found to be 1.42 V vs. RHE which is lower

than its onset potential (~1.49 V vs. RHE) in 1 M KOH electrolyte. This confirms that LCFO-10 exhibited excellent OER activity.

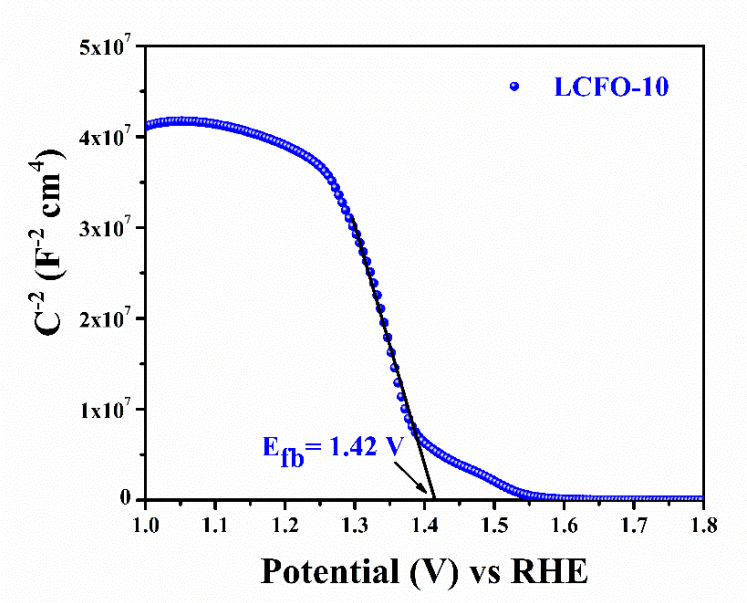

Figure 3.10 Mott-Schottky plot for LCFO-10 recorded at a frequency of 100 Hz.

3.3.4.4 Long-term stability Test

Electrochemical stability is an important factor to determine the practical application of the catalyst. The static stability of LCFO-10 was examined by performing a chronoamperometric (CA) measurement at 1.54 V vs. RHE for 12 h, shown in **Figure 3.11**. The CA plot indicates that LCFO-10 exhibits a current density of 10 mA cm^{-2} that slightly increases during the first few hours, after that, it was maintained throughout the experimental time scale. In addition, the dynamic stability of LCFO-10 was also checked by performing a thousand cycles of CV at a scan rate of 100 mV s^{-1} in the potential range of 1.0-1.8 V vs. RHE. The inset of **Figure 3.11** shows the LSV plots of the 1st, 100th, 500^{th,} and 1000th cycle of LCFO-10, and it was observed that there is only a marginal change in the overpotential at 10 mA cm^{-2} of LCFO-10 electrocatalyst, indicating its excellent stability in highly alkaline 1 M aqueous KOH electrolyte.

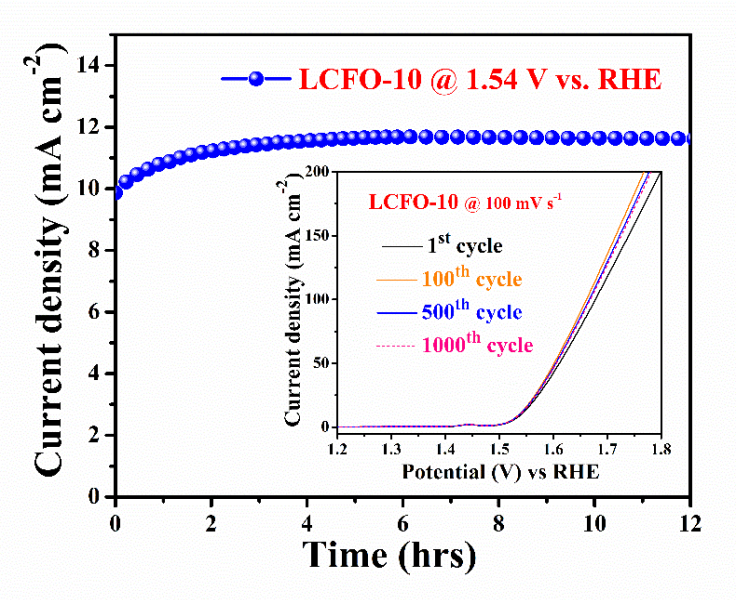

Figure 3.11 Chronoamperogram of LCFO-10 at an applied potential of 1.54 V vs. RHE for 12 hrs; inset shows the linear sweep voltammograms for the 1st, 100th, 500th and 1000th cycle at a scan rate of 100 mV s^{-1}.

3.3.4.5 Cyclic voltammograms for redox mechanism

To further explore the reason for the high electrocatalytic activity of the catalysts, we have performed CV scans in the range between 1.15 – 1.55 V vs. RHE in 1 M KOH electrolyte, shown in **Figure 3.12**. Previous studies had suggested that the active $LiMO_2$ catalysts exhibited a pre-OER redox peak that was attributed to in-situ electrochemical de-lithiation of the catalyst at higher oxidation potentials [15, 19]. In non-aqueous Li^+ electrolytes, $LiMO_2$ (M = Ni, Co, Cr, Mn) exhibited reversible Li^+ insertion/de-insertion in the range between 3.2 – 4.2 V vs. Li/Li^+ (or 0–1 V vs. Ag/ AgCl) [27, 35, 36]. However, the behavior of $LiMO_2$ in aqueous electrolytes is less reported, but in alkaline solutions, they exhibited reversible redox peaks of $M^{Z/Z+1}$ depending upon the pH of the electrolyte [36]. Hence, a lithium defect site can serve as an active site for the OER process in the $LiMO_2$ lattice. Furthermore, doping of Fe may enhance the Li-defect site in LCFOs, making them potentially more active as OER catalysts.

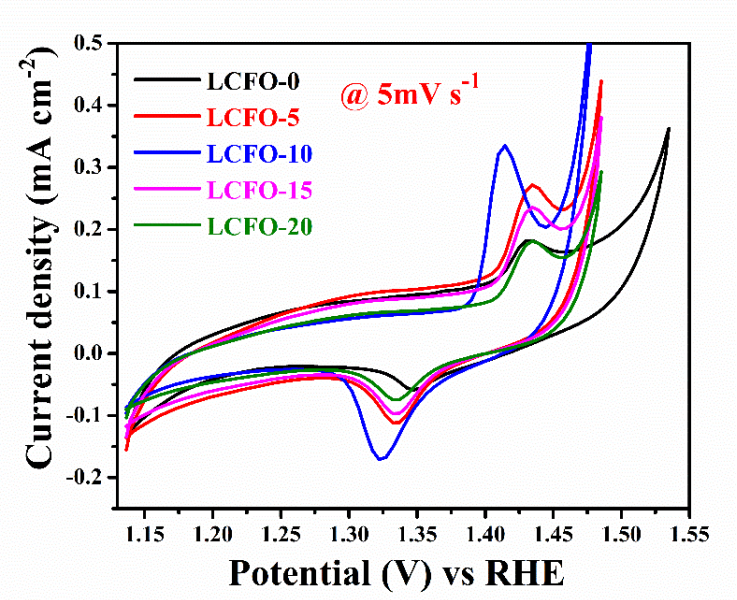

Figure 3.12 Cyclic voltammograms of $Li_yCr_{1-x}Fe_xO_2$ catalysts with various Fe contents ($y \leq 1$; $0 \leq x \leq 0.2$) recorded at a scan rate of 5 mV s^{-1} in 1 M KOH, demonstrating the effect of Fe-doping on the pre-OER redox peaks.

Figure 3.12 shows the cyclic voltammogram of different LCFO samples in the range between 1.15 – 1.55 V vs. RHE that consists of a pre-OER reversible redox peak. These faradaic features depict the in-situ activation of the electrocatalyst that is accompanied by the oxidation of Cr^{3+} to Cr^{6+}leading to Li-deficiency. A notable increase in the redox peak current at low onset potential (~1.42 and ~1.33 V vs. RHE for anodic and cathodic peaks, respectively) for $Cr^{3+/6+}$ redox couple LCFO-10 is a determining factor behind superior performance among all prepared LCFOs due to 3 electron transfer feasibility with single redox. The remarkable enhancement of OER performance may be attributed to the synergistic interaction of Cr and Fe as the Fe^{3+} ion-containing sample contain more Cr^{6+} ion in the lattice. A high-valence state of transition metal ion (Cr^{6+}) is responsible for its superior OER activity because it favours more adsorption of OH^- ion on the catalyst surface containing interstitial Cr ions that facilitate -Cr-O-OH formation [37]. As in basic solutions, Cr^{6+} is known to remain stable and -Cr-O-OH

(chromate ions) is very likely to form in high-pH alkaline solutions. The likely OER mechanism similar to Bockris`s electrochemical oxygen evolution route can be ascribed as:

$$S + OH^{-}(aq) \rightarrow \mathrm{S-OH} + e^{-} \quad (3.2)$$

$$S - OH + OH^{-}(aq) \rightarrow \mathrm{S-O^{\cdot}} + H_2O + e^{-} \quad (3.3)$$

$$2S - O^{\cdot} \rightarrow 2\mathrm{S} + O_2(\mathrm{g}) \quad (3.4)$$

where S is the surface-active dumbbell defect site (Cr^{6+}) of the catalyst.

3.3.5 Leaching experiment of LCFO-10 in HCl and KOH solution

To understand the stability and role of Cr^{6+} ions behind the superior activity of the catalyst, an acidic and basic leaching experiment with our synthesized LCFO-10 catalyst was further performed. First, 100 mg of catalyst in each of 50 ml of 1 M aq. HCl (acidic) and 10 M aq. KOH (basic) solution was continuously stirred for 5-6 h, and followed by resting in the same solution for 24 h. The sample solutions were then centrifuged and washed several times to remove the impurities from the recovered catalysts and dried in a hot air oven at 80 ℃ for 24 h. The recovered catalysts (HCl and KOH-treated LCFO-10) were further used to perform electrocatalytic measurements in the under same experimental conditions. **Figure 3.13** shows the OER performance of HCl and KOH-treated LCFO-10 and compared their results with as prepared LCFO-10 catalyst. From LSV curves as shown in **Figure 3.13a**, it was seen that an early onset potential of ~1.49 V vs. RHE is observed for as-prepared LCFO-10 compared to LCFO-10 treated with KOH and HCl. The overpotential for as-prepared LCFO-10 (311 mV) is achieved at 10 mA cm^{-2}, which is quite lower than that of LCFO-10 treated in KOH (376 mV) and LCFO-10 treated in HCl (407 mV). In addition, the Tafel plot and Nyquist plot were also presented in **Figure 3.13(b, c)**, separately. The lower value of Tafel slope and charge transfer resistance (R_{ct}) for as prepared LCFO-10 clearly indicates the superiority of our synthesized catalyst (LCFO-10). **Figure 3.13d** shows the pre-OER region of KOH and HCl

treated LCFO-10 samples along with as-prepared LCFO-10 in the potential range of 1.15-1.55 V vs. RHE. As mentioned above, the pre-OER redox peak for as prepared LCFO-10 occurs at a very low onset potential with the highest current density among all LCFOs. This redox peak is associated with Cr^{3+} to Cr^{6+} redox couples. Similarly, higher redox energies such as $Mn^{3+/4+}$, $Co^{3+/4+}$, $Ni^{3+/4+}$, and $Cr^{3+/6+}$ are known to be accessible in various $LiMO_2$ in the layered structure [15, 19, 38]. In the case of KOH-treated LCFO-10, this pre-OER redox peak considerably decreases and shifted to higher potentials unlike in the case of HCl-treated LCFO-10, where they disappear.

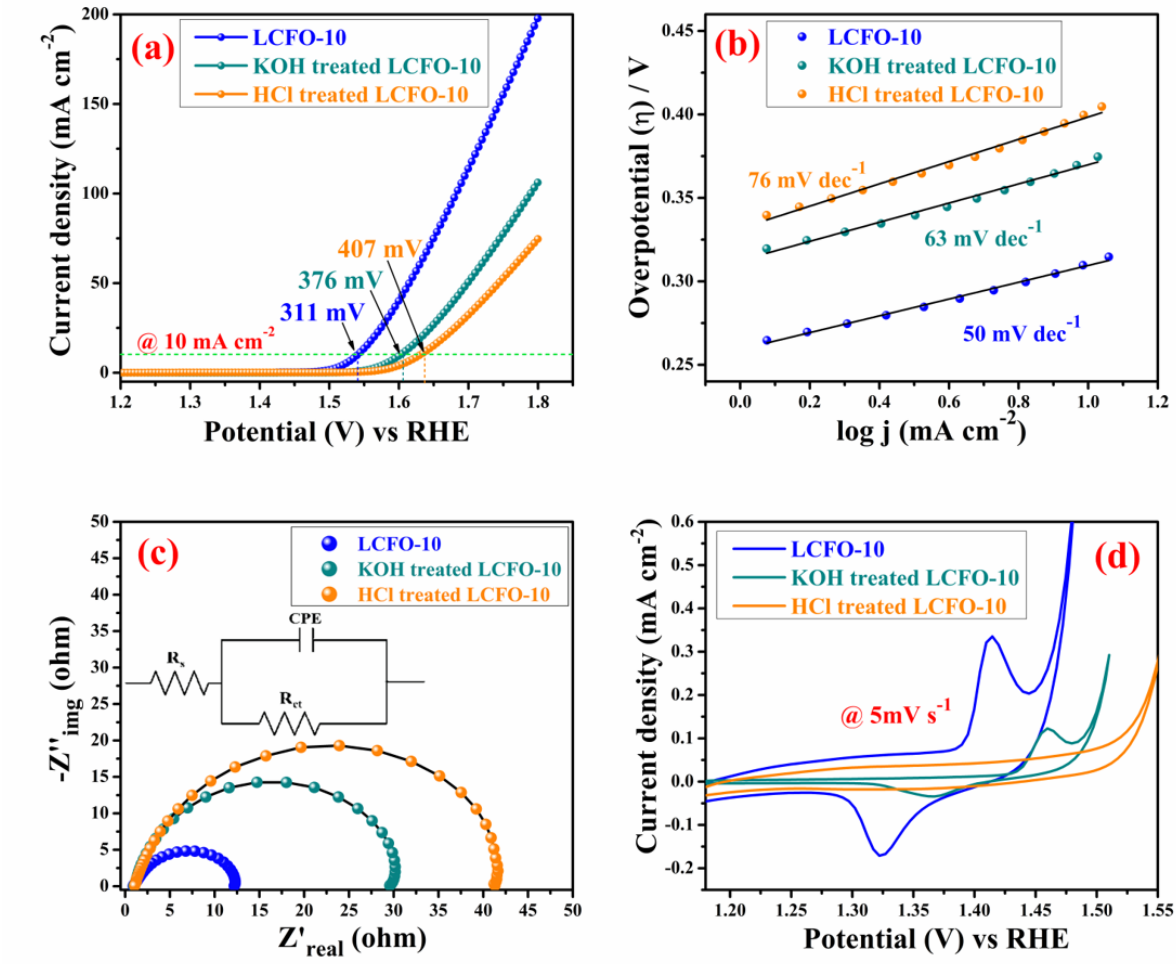

Figure 3.13 (a) Linear sweep voltammograms recorded at 5 mV s^{-1} in 1 M KOH, **(b)** Tafel plots, **(c)** EIS measurement at an applied potential of 1.54 V vs. RHE and **(d)** Cyclic voltammograms recorded at 5 mV s^{-1} shows the pre-OER region (1.15-1.55 V vs. RHE) of as prepared, KOH and HCl treated LCFO-10.

3.3.6 FTIR studies

Further, the formation of the CrO_4^{2-} ion or the presence of the Cr^{6+} ion in LCFO-10 was confirmed through the FTIR analysis. **Figure 3.14a** shows the FT-IR spectra of as-prepared, KOH and HCl-treated LCFO-10 samples in the range of 400–4000 cm^{-1}, & **Figure 3.14b** shows the close-up of the 400-1000 cm^{-1} region. In general, metal oxides reveal absorption bands below 1000 cm^{-1} due to the inter-atomic vibrations. The peaks located in the region of 400–800 cm^{-1} correspond to the stretching and bending vibrations of the Cr-O and Fe-O bond. Whereas, the peak located in the region of 800-950 cm^{-1} is attributed to CrO_4^{2-} vibration [39-43]. The band appeared at 1635 and 3250 cm^{-1} due to the O-H bending and O-H stretching vibrations also observed respectively. From **Figure 3.14b**, it has been observed that the peak located in the CrO_4^{2-} region (800-950 cm^{-1}) shows a decrease and shifted to a higher wavenumber, in the case of KOH and HCl-treated LCFO-10 compared to as prepared LCFO-10. This result confirms the CrO_4^{2-}ion or Cr^{6+} ions at the dumbbell interstitial sites of the HCP lattice.

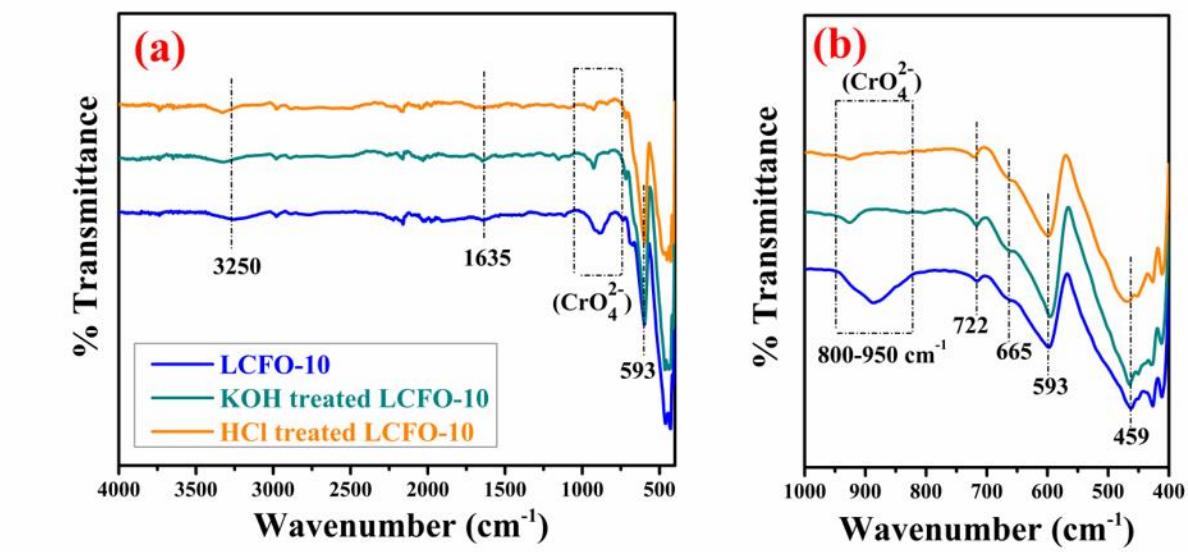

Figure 3.14 (a) Full range (400-4000 cm^{-1}) FT-IR spectra of as prepared, KOH and HCl treated LCFO-10 and **(b)** close-up of the 400-1000 cm^{-1} region.

3.3.7 Post OER characterization

Further, the post-OER characterizations (such as XRD, SEM, TEM, FT-IR, and XPS) were carried out to see the effect of electrochemical cycling on the microstructure of the synthesized catalyst (LCFO-10). The post-OER XRD of the LCFO-10 electrode shows no appreciable changes in the diffraction pattern, except for the peak of carbon paper (CP), and is well indexed to the standard rhombohedral phase (Space Group: R-3m) of $LiCrO_2$ (JCPDS No. 00-024-0600). However, the intensity ratio of the (003) to (104) peak decreases from 1.02 to 0.8, indicating some Li^+ ions are extracted during the electrochemical cycling **(Figure 3.15)**.

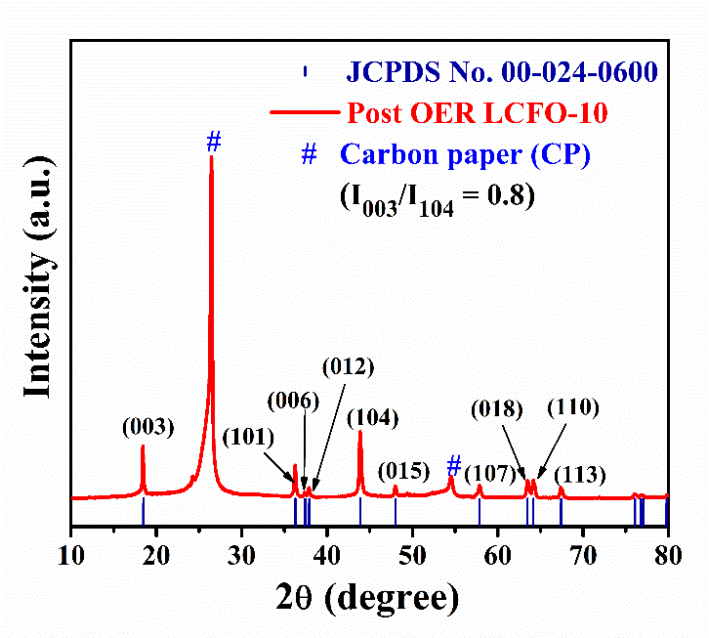

Figure 3.15 Post OER XRD pattern of LCFO-10 electrode.

The post-OER SEM images of the LCFO-10 electrode reveal that the morphology is maintained even after long-term anodic cycling **(Figure 3.16a, b)**. In addition, the post-OER elemental mapping images demonstrate the existence of Cr, Fe, C, and O elements in the LCFO-10 electrode **(Figure 3.16c-h)**. The microstructural study of the catalyst (LCFO-10) after a long-term stability test was further carried out via HR-TEM and SAED analysis. **Figure**

3.17(a, b) shows low to high magnified post-OER HR-TEM micrograph of electrode material (with the inset of SAED pattern in **Figure 3.17a**). The HR-TEM image **(Figure 3.17a** shows a lattice fringe with the calculated interplanar d-spacing of 0.25 nm corresponding to the (101) plane of the standard rhombohedral phase (Space Group: R-3m). The SAED pattern (inset of **Figure 3.17b**) shows distinct ring patterns indexed to (003), (101), (012), (104), and (015) plane of the rhombohedral phase of $LiCrO_2$, which is consistent with the post-OER XRD result **(Figure 3.15)**. These observations clearly confirm that the microstructural stability of the catalyst is retained even after long-term electrochemical testing.

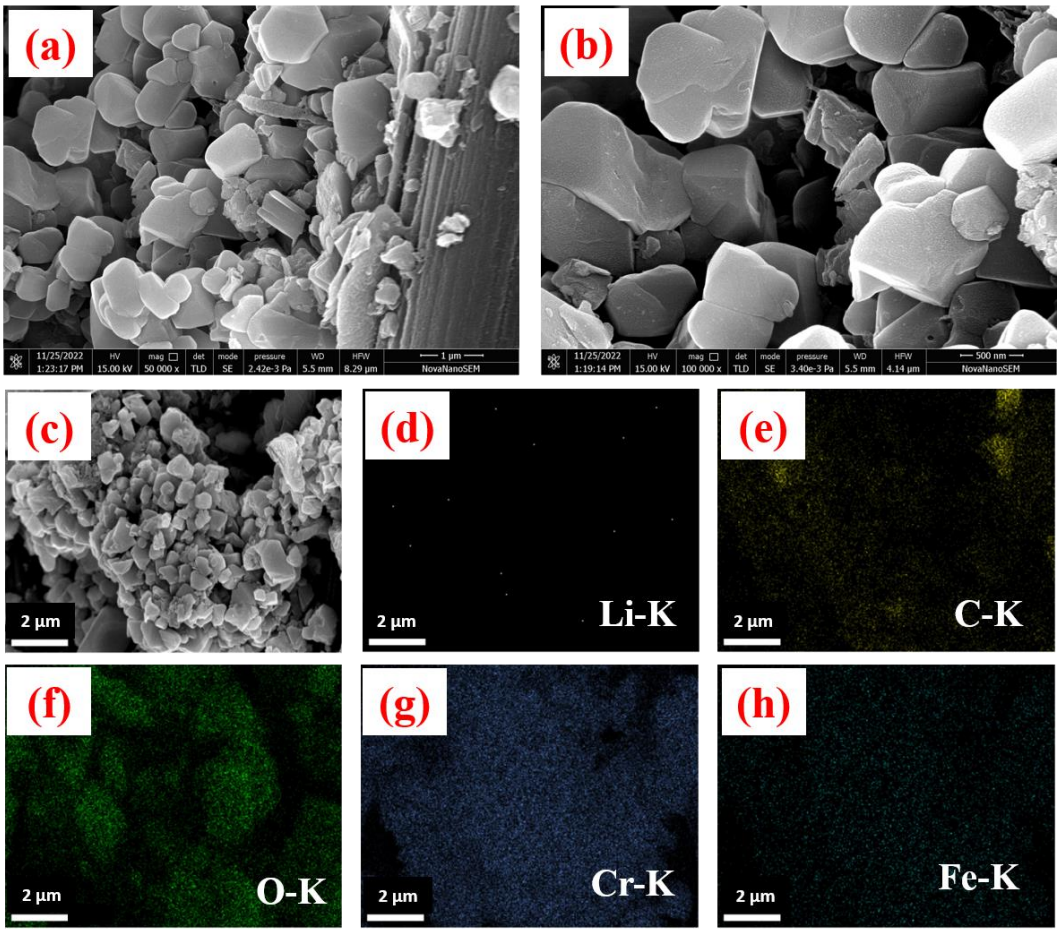

Figure 3.16 (a, b) Post OER SEM images of LCFO-10 electrode (Scale bar: **(a)** 1µm with 50,000x magnification and **(b)** 500 nm with 100,000x magnification) and **(c-h)** corresponding element mappings in LCFO-10 electrode. Note: Li signals are absent in EDX mapping as EDX techniques are not capable of recording signals for the Li core level.

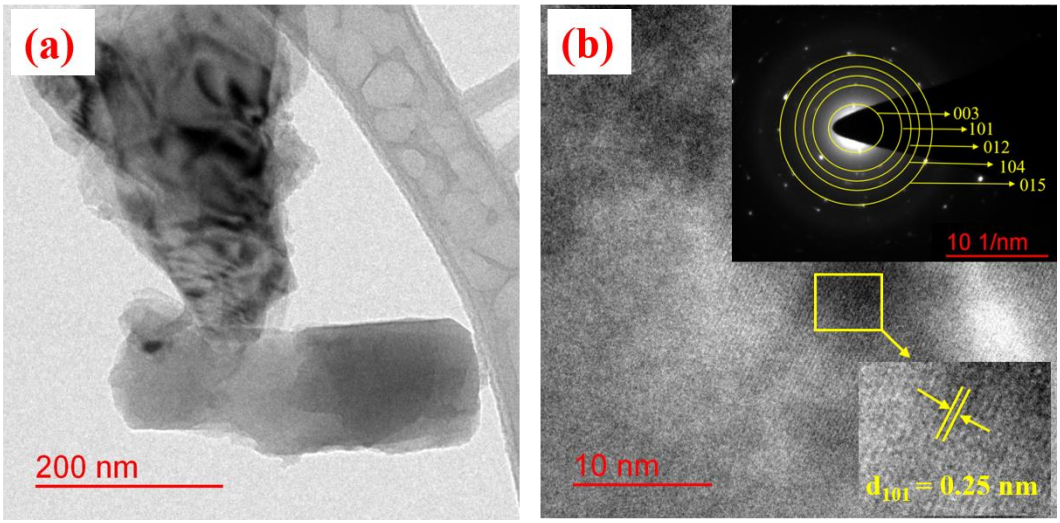

Figure 3.17 (a, b) Post-OER HR-TEM images of LCFO-10.

The post-OER FT-IR analysis, shown in **Figure 3.18,** confirms the formation of -Cr-O-OH during electrochemical cycling. The FT-IR absorption spectra of post-OER LCFO-10 exhibit strong absorption bands as compared to the pre-OER LCFO-10 (as prepared). The appearance of two additional bands at 1190 and 2017 cm^{-1} corroborates the presence of -Cr-O-OH. The strong peak observed at 1190 cm^{-1} corresponds to the Cr^{3+}—O—H bending vibration and broadband in the region between 1700-2100 cm^{-1} was assigned to the O—H stretching vibration in the OHO group of -Cr-OOH. These bands corresponded to typical frequencies of -Cr-O-OH [44-46]. The chemical nature or electronic structure of Cr was analyzed via XPS measurement of pre- and post-OER LCFO-10 electrodes and the resultant Cr(2*p*) spectra after deconvolution are presented in **Figure 3.19(a, b)**. The Cr(2*p*) peaks that correspond to Cr^{3+} and Cr^{6+} states are still observed at their respective binding energy region **(Table 3.3)** [27]. However, the concentration of Cr^{6+} has been increased in post-OER catalysts compared to those observed before, which is obvious as we have subjected the catalyst to a high anodic potential for a long time. This post-OER analysis confirms the stability of the catalyst that can become an alternative for efficient, cheaper, and long-lasting alternate OER catalyst for water electrolyzers.

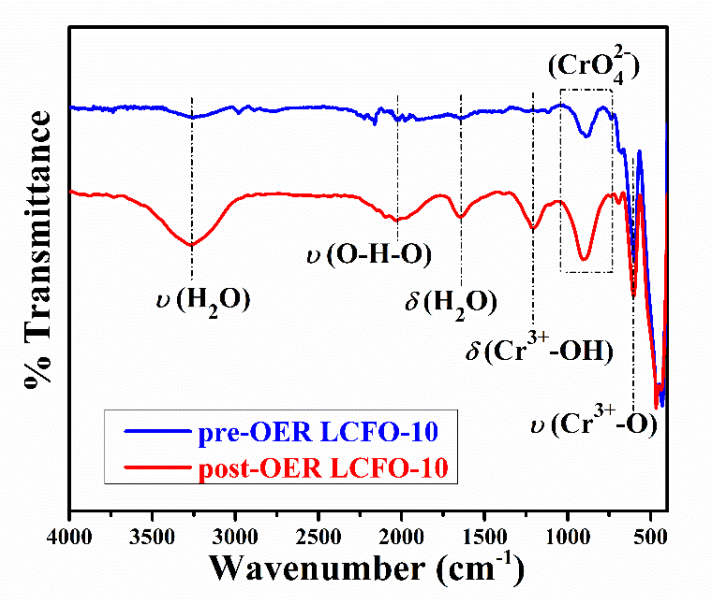

Figure 3.18 FTIR spectra of LCFO-10 before and after OER testing.

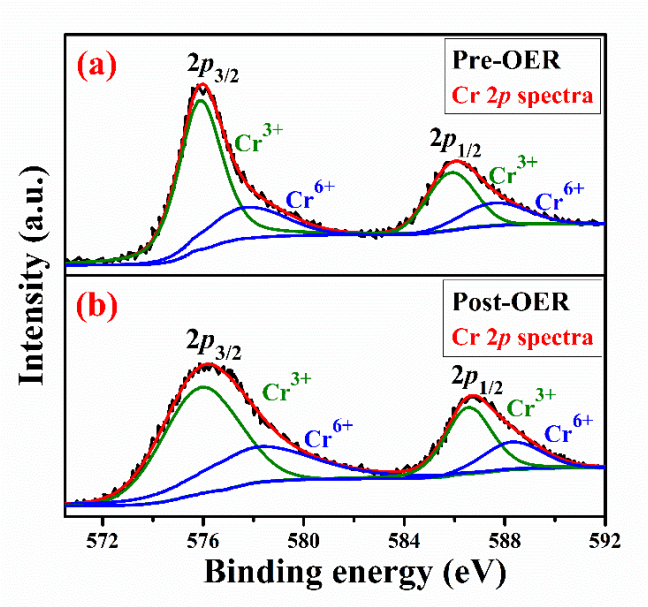

Figure 3.19 Cr 2p XPS spectra of LCFO-10 electrode **(a)** before testing (pre-OER) and **(b)** after testing (post-OER).

Table 3.3 Cr 2p XPS fitting data for pre- and post-OER LCFO-10 electrode material.

LCFO-10	Binding Energy (eV)			
	Cr $2p_{3/2}$		Cr $2p_{1/2}$	
	Cr^{3+}	Cr^{6+}	Cr^{3+}	Cr^{6+}
Pre-OER	575.9	577.8	585.8	587.6
Post-OER	576.03	578.26	586.5	588.3

3.4 Conclusion

Synthesis of lithium vacant chromium-rich dumbbell defect containing layered structure $Li_yCr_{1-x}Fe_xO_2$ ($y \leq 1$, $0 \leq x \leq 0.2$) due to occupancy of Cr^{6+} ions at interstitial tetrahedral sites present in hexagonal closed pack (HCP) rhombohedral lattice was achieved in solid state ceramic synthesis route in the oxygen environment. The presence of Cr^{6+} ions at the dumbbell interstitial sites of the HCP $LiCrO_2$ lattice was confirmed by XPS, FT-IR study, and the crystal structure of the materials was confirmed by powder XRD and HRTEM analysis. The superior electrocatalytic activity for OER was observed for Fe-doped $LiCrO_2$ samples. Whereas the electrocatalytic activity increases with increasing the Fe concentration up to 10%, after that the OER activity starts decreasing. The required overpotential to achieve a current density of 10 mA cm^{-2} (on a basis of 10% solar-to-fuel conversion efficiency) for LCFO-10, was found to be 311, and RuO_2 (a benchmark OER catalyst) requires a 336 mV overpotential to reach a current density of 10 mA cm^{-2}. At an overpotential of 350 mV, the OER current density of LCFO-10 is 28.07 mA cm^{-2}, which is ~2 times higher than OER current density observed with commercial RuO_2 (13.22 mA cm^{-2}), indicating its superior electrocatalytic activity. The remarkable enhancement of OER performance may be attributed to the synergistic interaction of Cr and Fe as the Fe^{3+} ion-containing sample contain more Cr^{6+} ion in the lattice. A high-valence state of transition metal ion (Cr^{6+}) is responsible for its superior OER activity because it favors more adsorption of OH^- ion on the catalyst surface containing interstitial Cr ions that facilitate -Cr-O-OH formation.

3.5 References

1. Ferreira, K.N., Iverson, T.M., Maghlaoui, K., Barber, J. and Iwata, S., 2004. Architecture of the photosynthetic oxygen-evolving center. *Science*, *303*(5665), pp.1831-1838.
2. Kanan, M.W. and Nocera, D.G., 2008. In situ formation of an oxygen-evolving catalyst in neutral water containing phosphate and Co^{2+}. *Science*, *321*(5892), pp.1072-1075.
3. Dau, H., Limberg, C., Reier, T., Risch, M., Roggan, S. and Strasser, P., 2010. The mechanism of water oxidation: from electrolysis via homogeneous to biological catalysis. *ChemCatChem*, *2*(7), pp.724-761.
4. Trasatti, S., 1980. Electrocatalysis by oxides—attempt at a unifying approach. *Journal of Electroanalytical Chemistry and Interfacial Electrochemistry*, *111*(1), pp.125-131.
5. Manchanda, R., Brudvig, G.W. and Crabtree, R.H., 1995. High-valent oxomanganese clusters: structural and mechanistic work relevant to the oxygen-evolving center in photosystem II. *Coordination Chemistry Reviews*, *144*, pp.1-38.
6. Dismukes, G.C., Brimblecombe, R., Felton, G.A., Pryadun, R.S., Sheats, J.E., Spiccia, L. and Swiegers, G.F., 2009. Development of bioinspired Mn_4O_4− cubane water oxidation catalysts: lessons from photosynthesis. *Accounts of Chemical Research*, *42*(12), pp.1935-1943.
7. Brimblecombe, R., Bond, A.M., Dismukes, G.C., Swiegers, G.F. and Spiccia, L., 2009. Electrochemical investigation of Mn_4O_4-cubane water-oxidizing clusters. *Physical Chemistry Chemical Physics*, *11*(30), pp.6441-6449.
8. Lyons, M.E. and Brandon, M.P., 2010. A comparative study of the oxygen evolution reaction on oxidised nickel, cobalt and iron electrodes in base. *Journal of Electroanalytical Chemistry*, *641*(1-2), pp.119-130.
9. Lyons, M.E. and Brandon, M.P., 2008. The oxygen evolution reaction on passive oxide covered transition metal electrodes in aqueous alkaline solution. Part 1-Nickel. *International Journal of Electrochemical Science*, *3*(12), pp.1386-1424.
10. Gao, M., Sheng, W., Zhuang, Z., Fang, Q., Gu, S., Jiang, J. and Yan, Y., 2014. Efficient water oxidation using nanostructured α-nickel-hydroxide as an electrocatalyst. *Journal of the American Chemical Society*, *136*(19), pp.7077-7084.
11. Jin, K., Seo, H., Hayashi, T., Balamurugan, M., Jeong, D., Go, Y.K., Hong, J.S., Cho, K.H., Kakizaki, H., Bonnet-Mercier, N. and Kim, M.G., 2017. Mechanistic investigation of water oxidation catalyzed by uniform, assembled MnO nanoparticles. *Journal of the American Chemical Society*, *139*(6), pp.2277-2285.

12. Koza, J.A., He, Z., Miller, A.S. and Switzer, J.A., 2012. Electrodeposition of Crystalline Co_3O_4 A Catalyst for the Oxygen Evolution Reaction. *Chemistry of Materials*, *24*(18), pp.3567-3573.
13. Trotochaud, L., Young, S.L., Ranney, J.K. and Boettcher, S.W., 2014. Nickel–iron oxyhydroxide oxygen-evolution electrocatalysts: the role of intentional and incidental iron incorporation. *Journal of the American Chemical Society*, *136*(18), pp.6744-6753.
14. Singh, R.N., Koenig, J.F., Poillerat, G. and Chartier, P., 1990. Electrochemical Studies on Protective Thin Co_3O_4 and $NiCo_2O_4$ Films Prepared on Titanium by Spray Pyrolysis for Oxygen Evolution. *Journal of The Electrochemical Society*, *137*(5), p.1408.
15. Suntivich, J., May, K.J., Gasteiger, H.A., Goodenough, J.B. and Shao-Horn, Y., 2011. A perovskite oxide optimized for oxygen evolution catalysis from molecular orbital principles. *Science*, *334*(6061), pp.1383-1385.
16. Augustyn, V. and Manthiram, A., 2015. Characterization of Layered $LiMO_2$ Oxides for the Oxygen Evolution Reaction of Metal–Air Batteries (M= Mn, Co, Ni). *ChemPlusChem*, *80*(2), pp.422-427.
17. Lee, S.W., Carlton, C., Risch, M., Surendranath, Y., Chen, S., Furutsuki, S., Yamada, A., Nocera, D.G. and Shao-Horn, Y., 2012. The nature of lithium battery materials under oxygen evolution reaction conditions. *Journal of the American Chemical Society*, *134*(41), pp.16959-16962.
18. Maiyalagan, T., Jarvis, K.A., Therese, S., Ferreira, P.J. and Manthiram, A., 2014. Spinel-type lithium cobalt oxide as a bifunctional electrocatalyst for the oxygen evolution and oxygen reduction reactions. *Nature communications*, *5*(1), p.3949.
19. Lu, Z., Wang, H., Kong, D., Yan, K., Hsu, P.C., Zheng, G., Yao, H., Liang, Z., Sun, X. and Cui, Y., 2014. Electrochemical tuning of layered lithium transition metal oxides for improvement of oxygen evolution reaction. *Nature communications*, *5*(1), p.4345.
20. Augustyn, V., Therese, S., Turner, T.C. and Manthiram, A., 2015. Nickel-rich layered $LiNi_{1-x}M_xO_2$ (M= Mn, Fe, and Co) electrocatalysts with high oxygen evolution reaction activity. *Journal of Materials Chemistry A*, *3*(32), pp.16604-16612.
21. Gupta, A., Chemelewski, W.D., Buddie Mullins, C. and Goodenough, J.B., 2015. High-rate oxygen evolution reaction on Al-doped $LiNiO_2$. *Advanced Materials*, *27*(39), pp.6063-6067.
22. Zhu, K., Wu, T., Zhu, Y., Li, X., Li, M., Lu, R., Wang, J., Zhu, X. and Yang, W., 2017. Layered Fe-substituted $LiNiO_2$ electrocatalysts for high-efficiency oxygen evolution reaction. *ACS Energy Letters*, *2*(7), pp.1654-1660.

23. Ye, W., Fang, X., Chen, X. and Yan, D., 2018. A three-dimensional nickel–chromium layered double hydroxide micro/nanosheet array as an efficient and stable bifunctional electrocatalyst for overall water splitting. *Nanoscale*, *10*(41), pp.19484-19491.
24. Kim, S., Ma, X., Ong, S.P. and Ceder, G., 2012. A comparison of destabilization mechanisms of the layered Na_xMO_2 and Li_xMO_2 compounds upon alkali de-intercalation. *Physical Chemistry Chemical Physics*, *14*(44), pp.15571-15578.
25. (a) Yang, Y., Dang, L., Shearer, M.J., Sheng, H., Li, W., Chen, J., Xiao, P., Zhang, Y., Hamers, R.J. and Jin, S., 2018. Highly active trimetallic NiFeCr layered double hydroxide electrocatalysts for oxygen evolution reaction. *Advanced Energy Materials*, *8*(15), p.1703189.

    (b) Sun, Z., Yuan, M., Yang, H., Lin, L., Jiang, H., Ge, S., Li, H., Sun, G., Ma, S. and Yang, X., 2019. 3D porous amorphous γ-CrOOH on Ni foam as bifunctional electrocatalyst for overall water splitting. *Inorganic Chemistry*, *58*(6), pp.4014-4018.
26. Gao, M., Ma, N., Yu, C. and Liu, Y., 2021. In situ synthesis of Fe-doped CrOOH nanosheets for efficient electrocatalytic water oxidation. *Nanotechnology*, *32*(28), p.28LT01.
27. Ohzuku, T., Ueda, A., Nagayama, M., Iwakoshi, Y. and Komori, H., 1993. Comparative study of $LiCoO_2$, $LiNi_{1/2}Co_{1/2}O_2$ and $LiNiO_2$ for 4 volt secondary lithium cells. *Electrochimica Acta*, *38*(9), pp.1159-1167.
28. Feng, G.X., Li, L.F., Liu, J.Y., Liu, N., Li, H., Yang, X.Q., Huang, X.J., Chen, L.Q., Nam, K.W. and Yoon, W.S., 2009. Enhanced electrochemical lithium storage activity of $LiCrO_2$ by size effect. *Journal of Materials Chemistry*, *19*(19), pp.2993-2998.
29. Cherkashinin, G., Nikolowski, K., Ehrenberg, H., Jacke, S., Dimesso, L. and Jaegermann, W., 2012. The stability of the SEI layer, surface composition and the oxidation state of transition metals at the electrolyte–cathode interface impacted by the electrochemical cycling: X-ray photoelectron spectroscopy investigation. *Physical Chemistry Chemical Physics*, *14*(35), pp.12321-12331.
30. Powell, C.J. and Larson, P.E., 1978. Quantitative surface analysis by X-ray photoelectron spectroscopy. *Applications of Surface Science*, *1*(2), pp.186-201.
31. Scofield, J.H., 1976. Hartree-Slater subshell photoionization cross-sections at 1254 and 1487 eV. *Journal of Electron Spectroscopy and Related Phenomena*, *8*(2), pp.129-137.
32. Penn, D.R., 1976. Quantitative chemical analysis by ESCA. *Journal of Electron Spectroscopy and Related Phenomena*, *9*(1), pp.29-40.

33. Anantharaj, S., Reddy, P.N. and Kundu, S., 2017. Core-oxidized amorphous cobalt phosphide nanostructures: an advanced and highly efficient oxygen evolution catalyst. *Inorganic Chemistry*, *56*(3), pp.1742-1756.
34. Jung, S., McCrory, C.C., Ferrer, I.M., Peters, J.C. and Jaramillo, T.F., 2016. Benchmarking nanoparticulate metal oxide electrocatalysts for the alkaline water oxidation reaction. *Journal of Materials Chemistry A*, *4*(8), pp.3068-3076.
35. Cheng, X., Fabbri, E., Yamashita, Y., Castelli, I.E., Kim, B., Uchida, M., Haumont, R., Puente-Orench, I. and Schmidt, T.J., 2018. Oxygen evolution reaction on perovskites: A multieffect descriptor study combining experimental and theoretical methods. *ACS Catalysis*, *8*(10), pp.9567-9578.
36. Rao, M.M., Liebenow, C., Jayalakshmi, M., Wulff, H., Guth, U. and Scholz, F., 2001. High-temperature combustion synthesis and electrochemical characterization of $LiNiO_2$, $LiCoO_2$ and $LiMn_2O_4$ for lithium-ion secondary batteries. *Journal of Solid State Electrochemistry*, *5*, pp.348-354.
37. Rao, M.M., Jayalakshmi, M., Schaff, O., Guth, U., Wulff, H. and Scholz, F., 1999. Electrochemical behaviour of solid lithium nickelate ($LiNiO_2$) in an aqueous electrolyte system. *J. Solid State Electrochem*, *4*, p.17.
38. Singh, R.N., Singh, J.P., Lal, B., Thomas, M.J.K. and Bera, S., 2006. New $NiFe_{2-x}Cr_xO_4$ spinel films for O_2 evolution in alkaline solutions. *Electrochimica acta*, *51*(25), pp.5515-5523.
39. Kim, S., Ma, X., Ong, S.P. and Ceder, G., 2012. A comparison of destabilization mechanisms of the layered Na_xMO_2 and Li_xMO_2 compounds upon alkali de-intercalation. *Physical Chemistry Chemical Physics*, *14*(44), pp.15571-15578.
40. Weckhuysen, B.M., Wachs, I.E. and Schoonheydt, R.A., 1996. Surface chemistry and spectroscopy of chromium in inorganic oxides. *Chemical Reviews*, *96*(8), pp.3327-3350.
41. Julien, C.M. and Massot, M., 2004, September. Vibrational spectroscopy of electrode materials for rechargeable lithium batteries: III. Oxide frameworks. In *Proceedings of the International Workshop Advanced Techniques for Energy Sources Investigation and Testing* (pp. 1-17).
42. Trivedi, M.K., Tallapragada, R.M., Branton, A., Trivedi, D., Nayak, G., Latiyal, O. and Jana, S., 2015. Characterization of physical, thermal and structural properties of chromium (VI) oxide powder: Impact of biofield treatment. *Powder Metallurgy & Mining*, *4*(1).
43. Monico, L., Janssens, K., Cotte, M., Sorace, L., Vanmeert, F., Brunetti, B.G. and Miliani, C., 2016. Chromium speciation methods and infrared spectroscopy for studying the

chemical reactivity of lead chromate-based pigments in oil medium. *Microchemical Journal*, *124*, pp.272-282.

44. Ratnasamy, P. and Leonard, A.J., 1972. Structural evolution of chromia. *The Journal of Physical Chemistry*, *76*(13), pp.1838-1843.
45. Bai, Y.L., Xu, H.B., Zhang, Y. and Li, Z.H., 2006. Reductive conversion of hexavalent chromium in the preparation of ultra-fine chromia powder. *Journal of Physics and Chemistry of Solids*, *67*(12), pp.2589-2595.
46. Liang, S.T., Zhang, H.L. and Xu, H.B., 2020. Preparation of hexagonal and amorphous chromium oxyhydroxides by facile hydrolysis of K_xCrO_y. *Transactions of Nonferrous Metals Society of China*, *30*(5), pp.1397-1405.